

Modification of Angular Velocity by Inhomogeneous MRI Growth in Protoplanetary Disks

M. T. Kato, K. Nakamura, R. Tandokoro

*Department of Earth and Planetary Science, Tokyo Institute of Technology, Ookayama
2-1-12-I2-10, Meguro-ku, Tokyo*

marikok@geo.titech.ac.jp

M. Fujimoto

*Institute of Space and Astronomical Science, Japan Aerospace Exploration Agency,
Yoshinodai 3-1-1, Sagamihara, Kanagawa*

and

S. Ida

*Department of Earth and Planetary Science, Tokyo Institute of Technology, Ookayama
2-1-12-I2-10, Meguro-ku, Tokyo*

ABSTRACT

We have investigated evolution of magneto-rotational instability (MRI) in protoplanetary disks that have radially non-uniform magnetic field such that stable and unstable regions coexist initially, and found that a zone in which the disk gas rotates with a super-Keplerian velocity emerges as a result of the non-uniformly growing MRI turbulence. We have carried out two-dimensional resistive MHD simulations with a shearing box model. We found that if the spatially averaged magnetic Reynolds number, which is determined by widths of the stable and unstable regions in the initial conditions and values of the resistivity, is smaller than unity, the original Keplerian shear flow is transformed to the quasi-steady flow such that more flattened (rigid-rotation in extreme cases) velocity profile emerges locally and the outer part of the profile tends to be super-Keplerian. Angular momentum and mass transfer due to temporally generated MRI turbulence in the initially unstable region is responsible for the transformation. In the local super-Keplerian region, migrations due to aerodynamic gas drag and tidal interaction with disk gas are reversed. The simulation setting corresponds to the regions near the outer and inner edges of a global MRI dead

zone in a disk. Therefore, the outer edge of dead zone, as well as the inner edge, would be a favorable site to accumulate dust particles to form planetesimals and retain planetary embryos against type I migration.

Subject headings: accretion disks — instabilities — MHD — planetary systems: formation — turbulence

1. Introduction

The ubiquity of extrasolar planets strongly suggests that planet formation is a common process associated with star formation. However, two serious barriers are recognized in planet formation theory: meter-size and type I migration barriers. Terrestrial planets or icy cores for gas giants that are embedded in protoplanetary disks tend to lose orbital angular momentum and migrate inward through tidal interaction with the disk gas (“type I migration”). Linear calculations (e.g., Tanaka et al. 2002) predict that the planets spiral into the host stars on timescales $\lesssim 10^5$ years for the minimum-mass solar nebula model, which is much shorter than observationally inferred disk lifetime. This is the type I migration barrier for survival of planets with an Earth mass or more.

The meter-size barrier is the barrier for formation of planetesimals. Since rotation speed of disk gas is slightly slower than dust grains or planetesimals due to negative radial pressure gradient due to global structure of the gas disk and the motions of meter-sized bodies (boulders) are marginally coupled to gas motion through aerodynamical gas drag, the meter-sized boulders suffer the fastest inward orbital migration and the timescale to spiral into the protostar is \sim a hundred orbits (Adachi 1976; Weidenschilling 1977). This timescale would be too short compared to the sticking timescale for the boulders to form planetesimals of 1–10 km radius or more, the motions of which are decoupled from the gas motion, since the meter-sized boulders are expected to stick together only poorly (Benz 2000).

One way to bypass the meter-size barrier is formation of clumps through self-gravitational instability of a dust layer, which can occur on orbital periods (Safronov 1969; Goldreich & Ward 1973). However, local Kelvin-Helmholtz instability due to difference in rotation velocities between the dust-rich layer (Keplerian) and an overlaying dust-poor layer (sub-Keplerian) would prevent dust grains from settling to the midplane to form the thin enough layer for the self-gravitational instability (Weidenschilling & Cuzzi 1993). Furthermore, if global turbulence exists in the disk, it also stirs up the dust grains from the midplane. Commonly observed strong $H\alpha$ emission from young stars implies protoplanetary disks are viscously

evolving accretion disks with turbulent viscosity. One of the most likely sources for the turbulence is magnetorotational instability (MRI) in weakly ionized disk gas (Balbus & Hawley 1991).

Although turbulence inhibits formation of the thin dust layer near the midplane, dust grains could be trapped into turbulent eddies. It is expected that meter-sized boulders are concentrated in anticyclonic eddies (e.g., Barge & Sommeria 1995; Chavanis 2000; Johansen et al. 2004; Inaba & Barge 2006). In particular, Johansen et al. (2007) carried out a simulation of evolution of self-gravitating boulders in an MRI turbulent disk and found that 1000km-sized clumps are formed in eddies. One of the biggest issues in this model is lifetime of eddies. To form clumps, the eddies must persist until boulders are accumulated into the eddies and produce highly dust-rich regions. Since rapid formation of highly dust-rich regions is required, Johansen et al. (2007) assumed meter-sized boulders that show the most favorable behavior in the disks.

Trapping of dust grains is also possible at a locally high-pressure disk radius, because a positive radial pressure gradient induces super-Keplerian gas flow in which dust grains suffer tail winds, while a normal negative gradient induces head winds (e.g., Nakagawa et al. 1986; Klahr & Lin 2005). Rice et al. (2004) demonstrated that meter-sized boulders can be accumulated in high-density spiral arms of self-gravitating disks.

The pressure maximum also exists near the inner boundary of MRI "dead" zone. Innermost disk regions are thermally ionized, so that MRI is active there. In outer regions, X rays from host stars and cosmic rays penetrate all the way to the midplane of the disk, and the ionization degree may be high enough to activate MRI. On the other hand, in the intermediate regions, only surface layers are MRI active and the regions near the midplane may be inactive ("dead") (Gammie 1996; Sano et al. 2000). Assuming steady gas accretion through a disk, disk gas surface density jumps up at the inner boundary of the dead zone according to the change in effective viscosity due to turbulence, so pressure maximum emerges there.

The pressure maximum, in other words, the outer boundary of a local super-Keplerian region also halts inward type I migration (Tanaka et al. 2002; Masset et al. 2006). If residual and/or secondary-generated dust grains maintain the dead zone when accretion of planetary embryos proceeds, the inner boundary of the dead zone is a favorable cite to retain planetary embryos. However, the inner boundary is generally located well inside 1AU. It cannot provide building blocks for terrestrial planets in habitable zones and icy planets nor retain the cores to form gas giants around solar-type stars, although it would play an important role in architecture of short-period extrasolar planets.

Kretke & Lin (2007), however, pointed out that a local dead zone can appear near the

ice line and the ice line can be a spatial barrier for dust migration due to gas drag. Because dust grains are the most efficient argents for charge recombination, ionization rates and thickness of the active layers rapidly decreases across the ice line due to condensation of icy dust grains. Correspondingly, in a range of disk accretion rates, a local dead zone appears near the ice line and at the outer boundary of the dead zone large amount of icy grains can be accumulated and cores are retained to form gas giants.

Brauer et al. (2008) performed simulations of dust settling and coagulation with radial migration due to gas drag and the ice line effect. They found that the dust to gas ratio increases and formation of planetesimals may be efficient near the ice line. Ida & Lin (2008a) showed that if the ionization rate is order of magnitude larger than that predicted by Kretke & Lin (2007) due to dust growth [Kretke & Lin (2007) assumed that all the dust grains have μm sizes], cores stop migration at the ice line and they efficiently form gas giants without significant reduction of type I migration speed. Note that in order for the ice line effect to actually work, disk accretion rate and dust population must be within some ranges of parameters such that the thickness of the active layer is comparable to that of dead zone near the ice line, although the ranges are not too restricted.

We here show through MHD simulations that the pressure maximum associated with quasi-steady local super-Keplerian rotation may be created in the MRI marginal regions, such as the outer boundary of the global dead zone as well as its inner boundary, without requirements of persistent turbulent eddies nor the ice line effect. The accumulation of dust grains and retention of planetary embryos at the outer boundary of the dead zone have a great importance for formation of terrestrial and jovian planets. MRI is controlled by the vertical component of magnetic field (B_z) penetrating the disks as well as by ionization degree (e.g., Sano et al. 2000). As shown in later sections, non-uniform temporal MRI turbulence that occurs in the marginally stable regions transforms disk gas flow into quasi-steady flow that has local rigid-rotation regions. This flow pattern is sustained by non-uniform pressure gradient produced by mass transfer associated with the temporal turbulence. In the outer regions of the local rigid-rotation regions, gas rotation is super-Keplerian.

Since dead zones may shrink as dust grains grow and surface areas for charge recombination decrease (Sano et al. 2000), such marginal state sweeps from outer disk regions to inner regions. Furthermore, the density fluctuations due to MRI turbulence induced by the enhanced ionization degree lead to disruptive collisions of small planetesimals and the collisions reproduce dust grains (Ida et al. 2008). The grains lower the ionization degree so that disk gas becomes marginally stable against MRI. Then, grain growth starts again. Thus, marginally MRI stable state could be maintained in significant regions at $\lesssim 10\text{AU}$ until disk gas is depleted to some degree (Ida et al. 2008). Oishi et al. (2007) showed the random

torques due to the density fluctuations in the surface active layers affect planetesimals in the dead zone near the disk midplane. This effect may result in more continuous dust production and help maintenance of the marginally stable state. Thus, it is expected that broad regions at $\lesssim 10\text{AU}$ may once experience such local super-Keplerian motions and accumulate dust grains to form planetesimals during disk evolution.

In section 2, we describe the numerical method and the initial conditions. We use a local shearing box with non-uniform B_z . In section 3.1, the results with a fiducial model are shown. In section 3.2, the dependence of the results on initial settings is presented. Summarizing the numerical results, we show in section 3.3 that creation of the rigid rotation and super-Keplerian regions is regulated by spatially averaged magnetic Reynolds number. Section 4 is conclusion and discussion.

2. Numerical Model

2.1. Shearing box model

We carry out local two-dimensional MHD simulations of protoplanetary disks in the shearing box model (Wisdom & Tremaine 1988; Hawley et al. 1995). The coordinates are centered at r_0 from a host star and rotating with Keplerian angular velocity at r_0 (Ω_0). The radial, azimuthal and vertical directions are x , y and z , respectively. Assuming uniformity in the y -direction, we simulate 2D flow in the x - z plane. From the flow in the x - z plane, the evolution of v_y is calculated. We will discuss coordinate sizes in the x - z directions (L_x and L_z) later. Periodic boundary conditions are applied for the x and z directions. In the x direction, Keplerian shear motion in the y -direction is taken into account in the boundary condition.

2.2. Basic equations

We adopt compressible resistive magnetohydrodynamic (MHD) equations:

$$\frac{\partial \mathbf{v}}{\partial t} + (\mathbf{v} \cdot \nabla) \mathbf{v} = -\frac{1}{\rho} \nabla \left(P + \frac{\mathbf{B}^2}{8\pi} \right) + \frac{1}{4\pi\rho} (\mathbf{B} \cdot \nabla) \mathbf{B} - 2\Omega_0 \times \mathbf{v} + 3\Omega_0^2 x \hat{\mathbf{x}}, \quad (1)$$

$$\frac{\partial \rho}{\partial t} + \nabla \cdot (\rho \mathbf{v}) = 0, \quad (2)$$

$$\frac{\partial \mathbf{B}}{\partial t} = \nabla \times [(\mathbf{v} \times \mathbf{B}) - \eta \nabla \times \mathbf{B}], \quad (3)$$

$$P = c_s^2 \rho, \quad (4)$$

where \mathbf{v} , P , ρ and c_s are velocity in the rotating frame, pressure, density and sound speed of the gas, respectively. The third and forth terms in r.h.s. of equation (1) are the Coriolis force and tidal force (the difference between the centrifugal force and gravitational force from the central star), in which $\hat{\mathbf{x}}$ is a unit vector in the x -direction. \mathbf{B} and η are magnetic field and resistivity. For simplicity, we omit the vertical component of the gravity. We include ohmic dissipation in equation (3), while we neglect ambipolar diffusion. Its effect is weaker than the ohmic dissipation in midplane of inner ($\lesssim 100\text{AU}$) disk regions (Jin 1996), although in the surface layer or disk inner edge, dissipation due to ambipolar diffusion may be important (Chiang & Murray-Clay 2007).

We scale length and time by disk scale height ($H = c_s/\Omega_0$) and Ω_0^{-1} , respectively. Then, the independent parameters in the equations are plasma beta (β) and magnetic Reynolds number (R_m) defined respectively by

$$\beta = \frac{2c_s^2}{v_A^2}, \quad (5)$$

$$R_m = \frac{v_{Az}^2}{\eta\Omega_0}, \quad (6)$$

where $v_A = B/\sqrt{4\pi\rho}$ is Alfven velocity and v_{Az} is its z -component. We assume spatially uniform and time-independent c_s and η .

We solve the resistive MHD equations using the CIP-MOCCT method (Yabe & Aoki 1991; Stone & Norman 1992) with grid sizes of $0.01H$ (for dependence of our results on resolution, see Appendix 1). We usually integrate the evolution until $t \simeq 100\Omega_0^{-1}$. Although most of numerical studies on nonlinear stages of MRI have assumed ideal MHD, we consider low ionization state with finite resistivity. Several numerical simulations (Fleming & Stone 2000; Hawley et al. 1996) showed that the finite magnetic resistivity reduces growth rates of the MRI.

2.3. Initial conditions

We assume that gas density is initially uniform (ρ_0), so pressure is also uniform (P_0) due to the assumption of isothermal gas (constant c_s). We also assign the initial value of plasma beta as $\beta = 400$ uniformly. According to the large β , we set initial steady flow as a uniform Keplerian shear flow, $v_y = -(3/2)x\Omega_0$.

The remaining parameter is R_m . This value determines the MRI growth rate (Jin 1996; Sano & Miyama 1999). For $R_m \lesssim 1$, short wavelength modes are stabilized by ohmic dissipation and the growth rate declines. For $\Omega_0 \propto r^{-3/2}$, the the most unstable wavelength

is (Sano & Miyama 1999)

$$\lambda_{\text{m.u.}} \simeq 2\pi \frac{\eta}{v_{\text{Az}}} \simeq \frac{2\sqrt{2}\pi}{\sqrt{\beta}R_{\text{m}}} H \simeq \frac{0.44}{R_{\text{m}}} H. \quad (7)$$

Since MRI would not occur in the disk if $H \lesssim \lambda_{\text{m.u.}}$, the stabilization condition is $R_{\text{m}} \lesssim R_{\text{m,crit}} \simeq 0.44$.

We consider marginally stable state for MRI, in which stable and unstable regions co-exist non-uniformly. In this study, we assume constant η , and the non-uniformity of R_{m} is set by that of v_{Az} (equivalently, B_z). Since non-uniform MRI is an essential point for the emergence of the super-Keplerian flow, similar results are obtained in the case of non-uniform η . We will show the results with non-uniform η in a next paper.

In order to represent the non-uniformity of B_z with uniform β , we set initial \mathbf{B}_0 such that

$$\mathbf{B}_0 = (0, B_0 \sin \theta, B_0 \cos \theta) \quad (8)$$

with uniform B_0 and non-uniform θ . As shown in Figure 1, we set $\theta = 0$ ($\cos \theta = 1$) in the middle region (unstable) with radial size L_{u} and $\theta = 85$ degrees ($\cos \theta \simeq 0.087$) in the side regions (stable) with individual radial size L_{s} . The box size in the horizontal direction is given by $L_x = L_{\text{u}} + 2L_{\text{s}}$. Transition zones between $\theta = 0$ and 85 degrees are set to avoid numerical instability. We include non-zero azimuthal magnetic component B_y because the plasma beta and therefore the magnetic pressure are set to be spatially uniform to establish the initial equilibration. The azimuthal component B_y is calculated even in these two-dimensional simulations on the x - z plane, but the assumption of axisymmetry excludes the occurrence of magnetic dynamo on the x - y plane due to reconnection of B_y and the results here do not change even if B_y is set to be zero. In our preliminary three-dimensional simulations, we find that the MRI growth due to reconnection of B_y in the side areas hardly affects the features of azimuthally averaged fluid motion. This is because the essential process of the transformation from Keplerian flow to quasi-steady non-uniform rotation flow is temporal MRI growth and the stabilization of MRI due to established rigid rotation but not due to dynamo of magnetic field (see section 3). The effects of three-dimensional flow will be addressed in detail in the next paper.

The above choice indeed situates both stable and unstable regions in the simulation box. Substituting equations (5) and (8) into equation (6), we obtain

$$R_{\text{m}} = \frac{v_{\text{A}}^2 \cos^2 \theta}{\eta \Omega_0} = \frac{2\beta^{-1} H^2 \Omega_0 \cos^2 \theta}{\eta} = 2.5 \left(\frac{\eta}{0.002 H^2 \Omega_0} \right)^{-1} \cos^2 \theta. \quad (9)$$

With a fiducial value $\eta = 0.002 H^2 \Omega_0$, MRI is initially activated ($R_{\text{m}} > R_{\text{m,crit}}$) in the middle region with $\theta < \theta_{\text{crit}} \simeq 65$ degrees. The exact dispersion relation (Appendix 2) show that

wavelengths of all the growing modes exceed the vertical box size L_z for $\theta < \theta_{\text{crit}} \simeq 79$ degrees. The vertical size L_z is set to be $\simeq 0.5H$ that is comparable to the most unstable wavelength $\lambda_{\text{m.u.}}$ (equation [7]).

We have carried out 79 runs in total with various η , L_u , and L_s . The detailed simulation parameters are given in Table 1. In some cases, we adopted larger values of η , in which $\lambda_{\text{m.u.}}$ is larger (equation [7]). Then, we adopt L_z as large as $\lambda_{\text{m.u.}}$ with $R_m \sim 1$. In all runs, random fluctuations are initially given in the velocity field with a maximum amplitude of $|\delta v_x| = 0.001c_s$.

3. Results

3.1. The Fiducial Model

We first present the detailed results from a fiducial model with $\eta = 0.002H^2\Omega_0$, $L_u = 1.43H$, $L_s = 4.05H$, and $L_z = 0.5H$. Compared with the other models, this model initially has the largest stable regions. If the whole region has uniform and strong enough magnetic field, MRI turbulence is self-sustaining. However, evolution of turbulence is quite different in the case of non-uniform magnetic field that we consider here. MRI turbulence appears only tentatively, but velocity field is transformed from Keplerian shear flow to another quasi-steady flow.

Time evolution of the magnetic field on the x - z plane is shown in Figure 2a. In the panel of $t\Omega_0 = 21$, the field lines start to be stretched only in the initially unstable region. At $t\Omega_0 = 27$, MRI turbulence develops and the turbulence is transported into the initially stable regions. Accordingly, the magnetic perturbations become weaker and eventually vanish before they reach the boundary of the computing box (before they fully fill the stable region).

Figure 2b shows evolution of B_z averaged over z . Turbulent diffusion smooths out B_z , however, its level does not go below the critical value for stabilization of MRI ($\sim 0.2B_0$) in the initially unstable region (the middle region) even at $t\Omega_0 = 70$. Nevertheless, MRI turbulence ceases after $t\Omega_0 \gtrsim 40$. This is because in the middle region, rigid rotation is realized as a result of the angular momentum transfer during the MRI turbulence there (Fig. 2c) and the free-energy source for MRI (differential rotation) is lost. In the other areas, B_z is smaller than the critical value and MRI does not grow. The stabilization due to rigid rotation is discussed with linear analysis in Appendix 2.

As shown in Figure 2a, the region of the rigid rotation expands as propagation of turbulence. This local rigid rotation is self-sustaining, at least, until the remaining B_z is

diffused out by ohmic dissipation on timescale $\sim L_u^2/\eta \sim 10^3\Omega_0$ (see discussion in section 4). As long as certain level of B_z is maintained, deviation from the rigid rotation excites MRI turbulence and this transfers angular momentum to bring the velocity profile back to the rigid rotation state.

Figure 2d is the vertically averaged pressure distribution. The MRI turbulence radially transports mass, associated with the angular momentum transfer. Since in the unstable region, mass transfer is efficient and gas density is proportional to pressure in our isothermal model, pressure is decreased in the unstable region while it is increased in the stable regions adjacent to the unstable region. The resultant pressure gradients near the boundaries between the stable and unstable regions equilibrates with the Coriolis and tidal forces raised by a deviation from Keplerian rotation. In Figure 3, we plot radial components of individual terms in the r.h.s. of the equation of motion (equation [1]) near the right boundary between the stable and unstable regions ($x/H = 0.7$, $z/H = 0.25$). At $t\Omega_0 = 20\text{--}40$, the amplitude of magnetic pressure and tension are increased by the development of MRI turbulence and gas pressure gradient is also raised according to mass transfer associated with the turbulence. After the MRI turbulence ceases, the pressure gradient almost equilibrates with the Coriolis and tidal forces. Thus, the rigid rotation with pressure variation caused by the MRI turbulence is quasi-steady.

As stated in section 1, dust grains can be trapped in outer edge of local super-Keplerian regions, because dust grains suffer tail wind and migration outward in the super-Keplerian regions (see sections 1 and 4) while they suffer head wind in the other sub-Keplerian regions. In the result of Figure 2, the super-Keplerian region exists at $0.0 < x/H \lesssim 2.0$ in the quasi-steady state.

3.2. Dependence on widths of stable and unstable regions

In the limit of $L_s \rightarrow 0$ or $L_u \rightarrow \infty$, the system would have uniform turbulence and would not acquire the local rigid rotation. To derive the condition for establishment of the local rigid rotation, we perform runs with different values of L_s and L_u .

In the fiducial case, $L_u = 1.4H$ and $L_s = 4.0H$. We first present the results of a series of runs with various values of L_s and the fixed L_u . In model-s11, model-s055, and model-s005, $L_s = 1.1H$, $0.55H$, and $0.05H$, respectively. The other parameters are the same as those in the fiducial model. Figure 4 describes the evolution of the magnetic field in model-s11. Since the stable region is narrower than the fiducial case, the magnetic perturbations that arise in the unstable region propagate to the boundary of the computational box before they

are dissipated. The whole region including the initially stable region becomes temporarily turbulent. However, the perturbations that reach the boundary are weakened and do not have enough momentum to go into the unstable region again. The turbulence ceases after $t\Omega_0 \gtrsim 40$ and the quasi-steady rigid rotation is obtained as the result, although the pressure contrast is smaller than that in the fiducial model (the minimum pressure is $\simeq 0.65P_0$, while it is $\simeq 0.33P_0$ in the fiducial model).

The evolution of the MRI in model-s055 is shown in Figure 5. The narrower stable region allows the magnetic perturbations to come back to the unstable region because of the periodic boundary condition. The turbulence lives longer, but it eventually vanishes by $t\Omega_0 \sim 70$. The quasi-steady velocity profile which is more flattened than the Keplerian is established, although it is not as distinctive as the rigid rotation in the fiducial model.

Figure 6 shows the result of model-s005. Because of the small stable regions, turbulence expanded to the entire region does not cease and uniform turbulence is maintained. Efficient angular momentum transfer in the entire region prevents velocity field from having a quasi-steady super-Keplerian region.

So far, we have changed values of L_s while L_u is constant. We also performed a run (model-u34) with $L_u = 3.4H$ that is enlarged from the fiducial model. The other parameters are the same as those in the fiducial model. The results are shown in Figure 7. In the enlarged unstable region, the magnetic field is stretched enough for reconnection. After the reconnection, long-lived magnetic perturbations are sustained around the boundary between unstable and stable regions (the panel at $t\Omega_0 = 58.5$). The magnetic perturbations reach the computational boundary, because the conversion from magnetic energy to kinetic energy during the magnetic reconnection adds horizontal motion to the fluid element. However, the magnetic perturbations are not strong enough to pass through the stable region and come back to the unstable region. As a result, the evolution is similar to model-s11, except that the rigid rotation is established in the regions near the boundary between unstable and stable regions. The panels at $t\Omega_0 = 61.5$ and $t\Omega_0 = 99.0$ show that this flow pattern is also quasi-steady.

These results suggest that dissipation of magnetic perturbations during the passage through stable regions plays an essential role in creation of rigid rotation regions. We performed additional series of runs with a larger value of the resistivity, $\eta = 0.0028\Omega_0 H^2$. The result of model- $\eta 0$ with $L_u = 1.4H$ and $L_s = 4.0H$ (the same as the fiducial model) is shown in Figure 8. Because of the faster dissipation, the quasi-steady rigid rotation is established more early, although the weaker angular momentum transfer leads to smaller pressure contrast in the quasi-steady state. Even if we reduce L_s to $\sim 0.5H$, the magnetic perturbations do not arrive at the boundary. We also performed runs with further larger values of the

resistivity, $\eta/(\Omega_0 H^2) = 0.0012, 0.0036, 0.0044, 0.0052$ and 0.0060 (Table 1) to confirm that the quasi-steady rigid rotation is always established for these values of η . We discuss the dependence on the resistivity in the next subsection.

3.3. Condition for the rigid rotation

As we have shown, establishment of the quasi-steady rigid rotation depends on L_u , L_s , and η . Through the results with various L_u , L_s , and η as listed in Table 1, we found that the results are summarized by a single parameter, a spatially averaged magnetic Reynolds number, defined by (Sano & Miyama 1999; Sano & Inutsuka 2004)

$$R_{m,ave} = \frac{v_{Az,ave}^2}{\eta \Omega_0}, \quad (10)$$

where $v_{Az,ave}$ is evaluated by a spatially averaged vertical magnetic field ($B_{z,ave}$) at the initial stage. In our simulation setting, $B_{z,ave} \simeq B_0(L_u + 2 \cos 85^\circ L_s)/(L_u + 2L_s)$.

In many cases, the initial distributions of vertical magnetic field are spatially smoothed out by turbulent diffusion after ~ 10 orbits. If the remaining magnetic field ($\sim B_{z,ave}$) is still large enough to globally cause MRI turbulence, the transition to the quasi-steady state does not occur, as seen in the results of model-s005. Linear theory shows that the critical magnetic Reynolds number for occurrence of MRI is $R_m \sim 1$ (Sano & Miyama 1999; Sano & Inutsuka 2004). Thus, $R_{m,ave}$ regulates the establishment of the quasi-steady rigid rotation in our simulations.

We summarize the results of 91 runs with different parameters in Figure 9 and found that evolution of the magnetic field is indeed classified into four types by the values of $R_{m,ave}$ as follows:

Type A ($R_{m,ave} \lesssim 0.1$): Local MRI turbulence generated in the initially unstable region propagates both inward and outward, but the magnetic perturbations are dissipated before they reach the boundary of the simulation box. After a few tens of orbits, the turbulence vanishes in the entire region and the quasi-steady flow is established. In the initially unstable region, rigid rotation flow is resulted in by angular momentum transfer due to the MRI turbulence. This class is represented by filled circles in Figure 9 and it includes the fiducial model and model- $\eta 0$.

Type B ($0.1 \lesssim R_{m,ave} \lesssim 0.5$): The magnetic perturbations reach the boundary, but they do not intrude back into the original unstable region. The quasi-steady rigid-rotation

region appears as in Type A. This class is represented by triangles in Figure 9 and it includes model-s11 and model-u34.

Type C ($0.5 \lesssim R_{\text{m,ave}} \lesssim 1.0$): The magnetic perturbations intrude the unstable region after the passage through the stable regions. However, the diffused B_z is not large enough to globally maintain turbulence and the quasi-steady rigid rotation region is still formed, although their locations are not necessarily the same as in Type A and B. This class is represented by daggers in Figure 9 and it includes model-s055.

Type D ($1.0 \lesssim R_{\text{m,ave}}$): Even after the turbulent diffusion, B_z is able to maintain the turbulence in the entire region. Because of the uniform turbulent state, the quasi-steady rigid rotation state is not generated. This class is represented by crosses in Figure 9 and it includes model-s005.

4. Conclusion and Discussion

We have investigated evolution of patchy magneto-rotational instability (MRI) due to radially non-uniform magnetic field and found that, under some conditions, the original Keplerian shear flow is transformed into quasi-steady profile involving a local rigid-rotation regions. The outer parts of the rigid-rotation regions are generally super-Keplerian. Such a situation would arise in the outer boundary of MRI dead zone as well as the inner boundary in a protoplanetary disk, as discussed in section 1.

Assuming uniformity in the azimuthal direction of disks, we have carried out two-dimensional resistive MHD simulations in a shearing box model with periodic boundary conditions. We set up both stable and unstable regions in the box, changing direction of the vertical seed magnetic field (B_z) non-uniformly. In the initially unstable region, MRI turbulence is generated locally and magnetic perturbations propagate both radially inward and outward by the turbulent diffusion. If the unstable region is sufficiently large compared with the stable region, the turbulence eventually covers the entire region and the initial non-uniformity vanishes. However, if the stable region is relatively large, diffused magnetic perturbations no more maintain MRI turbulence. After the turbulence ceases, the initial flow of uniform Keplerian shear is transformed into a different quasi-steady state. In the quasi-steady state, rigid-rotation is established locally. The deviation from Keplerian shear motion is supported by pressure gradient that has been produced also by mass transport associated with the tentative turbulence. Through simulations with various initial conditions, we found that the quasi-steady rigid rotation is established if the spatially averaged magnetic Reynolds number satisfies $R_{\text{m,ave}} \lesssim 1$ in the initial state.

Because the center of the local rigid rotation is often Keplerian, super-Keplerian flow appears in the outer parts of the rigid rotation region. As explained in section 1, dust grains and planetary embryos can be trapped in the boundary between regions of sub- and super-Keplerian motion through radial migration induced by aerodynamic gas drag and type I migration. The boundary is coincident with pressure maxima in the quasi-steady state.

The effect of global pressure gradient is included by shifting the initial gas velocity from the pure Keplerian speed to slight sub-Kepler. The shift, which is the velocity difference between the disk gas and the dust grains, is (e.g., Adachi 1976; Weidenschilling 1977)

$$\Delta v_y = \frac{c_s^2}{2v_K^2} \frac{d \ln P}{d \ln r} v_K \simeq -5 \times 10^{-2} \left(\frac{r}{1 \text{AU}} \right)^{3/4} c_s \quad (11)$$

where $d \ln P / d \ln r$ is the global pressure gradient and the temperature distribution in the limit of optically thin disks around solar-luminosity stars, $T = 280(r/1\text{AU})^{-1/2}$, is assumed. Since maximum values of Δv_y in the super-Keplerian regions are $\gtrsim 0.4c_s$ in our results, the MRI effects can easily surpass the global pressure gradient effects and super-Keplerian regions can emerge even when the initial down-shift in the gas rotation velocity is present.

If the super-Keplerian region is sustained long enough for dust grains to accumulate, planetesimals can be formed through self-gravitational instability (Youdin & Shu 2002; Johansen et al. 2006). In the case of $R_{\text{m,ave}} \lesssim 1$ in which MRI turbulence ceases in the entire region after a few tens of orbits, we found that B_z is still large enough in the rigid-rotation region. In that region, MRI is suppressed by disappearance of shear motion but not by dissipation of B_z (in the regions other than the rigid-rotation region, diffused-out B_z is smaller than the value for MRI to occur). If the rigid rotation tries to go back to the original Keplerian shear motion, MRI turbulence again occurs and it transfers angular momentum to recover the rigid rotation. Thus, the rigid rotation and hence the associated super-Keplerian rotation are self-sustaining. When the remaining B_z is diffused out by ohmic dissipation on timescale $\sim L_u^2/\eta \sim 10^3 \Omega_0^{-1}$, such stabilization mechanism is no more effective. Then, the rigid rotation can go back to the original Keplerian shear motion by the residual uniform viscosity. However, since MRI no more occurs, the residual viscosity would be very small. Thus, it is expected that the super-Keplerian regions would survive long enough for accumulation of dust grains and formation of planetesimals. We also did a calculation starting from the end result of the super-Keplerian rotation state, artificially modifying B_z to uniform distribution. However, we do not see any relaxation of the velocity field back to Keplerian rotation within the timescales of 40 orbits.

In the next paper, we will demonstrate the accumulation of dust grains and discuss the effect of the azimuthal magnetic field especially in stable region by three-dimensional simulation. We will also show the results of non-uniform resistivity case with constant B_z , which

may be more likely to occur at the outer edge of a dead zone. We find similar appearance of super-Keplerian regions, because intrinsic physics to transform initial Keplerian flow to quasi-steady non-uniform rotation flow is temporal generation of MRI and the stabilization of the MRI due to the established rigid rotation but not due to dynamo of magnetic field (see section 3).

The appearance of the super-Keplerian region also halts inward type I migration of planetary embryos (Tanaka et al. 2002; Masset et al. 2006). Since the process we found also works at the outer boundary of a dead zone and the outer boundary migrate from $\sim 10\text{AU}$ to the proximity of the central star, this process may also help the formation of cores massive enough to onset runaway gas accretion and retain terrestrial planets against type I migration. This may play an important role in frequency of extrasolar gas giants and habitable planets. We will address this issue with sequential planet formation model (Ida & Lin 2004, 2008a,b) in a future paper.

We thank detailed helpful comments by an anonymous referee.

Appendix 1. Resolution test

We have investigated the effects of numerical resolution on our results using our fiducial model. Four cases are studied. The distribution of angular velocity and the average Maxwell stress are shown in Figure 10. The most important issue in our results is the emergence of the quasi-steady state in which sub- and super-Keplerian areas exist. Figure 10a shows this to be seen even in the worst resolution case. In addition, the Maxwell stress in Figure 10b appears to be converging at resolutions above $dx = 0.01H$ while this quantity tends to increase with resolution.

Fromang & Papaloizou (2007) showed the decrease of Maxwell stress with increasing resolution and stated that the MRI turbulence activity is notoriously ill-behaved in high resolution calculation. Our resolution test, however, shows the convergence with increasing resolution. This could be because the ohmic dissipation (resistivity) is kept constant in our resistive MHD simulations while the simulation of Fromang & Papaloizou (2007) included only the numerical resistivity and it decreases with increasing resolution. However, more detailed study is needed to clarify the difference in convergence between our simulation and the simulation of Fromang & Papaloizou (2007), which is left to our future study.

This fact will be important when we investigate the motion of dust particles. The degree of particle concentration may be depend on the turbulence activity. While the details are left for a future study, one may reasonably expect the possibility of dust concentration at

the outer-edge of super-Keplerian area.

Figure 10b also shows the eligibility of the integration time. The saturation level varies only slightly in $t\Omega_0 > 60.0$ in the two high resolution cases. The quasi-steady state has already been created by this time. These indicate that our choice the integration time $t\Omega < 100.0$ is validated.

Appendix 2. Dispersion relations

Our simulations show that the MRI stabilization in strong magnetic field with nearly rigid rotation, which is consistent with the linear analyses. The linear analysis using ideal MHD equations in Balbus & Hawley (1991) gave the critical wavelength (equation (2.14b) in the paper, with neglect of the Brunt-Väisälä frequency):

$$|\lambda_{z,\text{crit}}| = v_{Az} \left| \frac{d\Omega^2}{d \ln r} \right|^{-1/2} = \frac{v_{Az}}{\Omega} (2|q|)^{-1/2}, \quad (1)$$

where q is defined as $\Omega(r) \propto r^{-q}$. The perturbations with wavelength shorter than $\lambda_{z,\text{crit}}$ are stable. When the rotation becomes rigid rotation ($q \rightarrow 0$), $\lambda_{z,\text{crit}}$ becomes large. If $\lambda_{z,\text{crit}}$ is larger than the scale height of a disk, the system is stable, irrespective of magnetic field strength.

With the effect of ohmic dissipation, the dispersion relation was obtained by Jin (1996) and Sano & Miyama (1999) as

$$\sigma^4 + 2\xi\sigma^3 + \left(2q_z^2 + \xi^2 + \frac{\kappa^2}{\Omega^2}\right)\sigma^2 + 2\xi\left(q_z^2 + \frac{\kappa^2}{\Omega^2}\right)\sigma + \left(-4 + \frac{\kappa^2}{\Omega^2}\right)q_z^2 + q_z^4 + \frac{\kappa^2}{\Omega^2}\xi^2 = 0, \quad (2)$$

where σ is a growth rate in units of orbital frequency, $q_z = k_z v_{Az}/\Omega$, $\xi = k_z^2 \eta/\Omega$, and κ is an epicyclic frequency defined by

$$\kappa^2 = \frac{2\Omega}{r} \frac{d(r^2\Omega)}{dr} = (2 - q) 2\Omega^2. \quad (3)$$

This dispersion relation is derived with the assumption of uniform density and negligible Brunt-Väisälä frequency. Since the density is almost uniform in the rigid rotation in our simulation, we apply this dispersion relation to calculate the predicted σ with the quantities obtained by our simulation. We plot the temporally and vertically averaged q ($= -dv_x/dx$), Maxwell stress ($-\langle B_x B_y \rangle / 4\pi P_0$) and the evaluated growth rate σ in Figure 11. The growth rate is very small in the middle region of nearly rigid rotation ($q \ll 1$), although Maxwell stress is not small there. Thus, we conclude that MRI is suppressed by established nearly rigid rotation, but not by dissipation of magnetic field.

REFERENCES

- Adachi, I., Hayashi, C., & Nakazawa, K. 1976, *Prog. Theor. Phys*, 56, 1756
- Balbus, S. A., & Hawley, J. F. 1991, *ApJS*, 376, 214
- Barge, P., & Sommeria, J. 1995, *A&A*, 295, L1
- Benz, W. 2000, *Space Sci. Rev.*, 92, 279
- Brauer, F., Henning, Th., & Dullemond, C. P. 2008, *A&Aaccepted*
- Chavanis, P. H. 2000, *A&A*, 356, 1089
- Chiang, E. I., & Murray-Cley, R. A. 2007, *Nature Phys.*, 3, 604
- Fleming, T. P., Stone, J. M., & Hawley, J. F. 2000, *ApJS*, 530, 464
- Fromang, S., & Papaloizou, J. 2007, *A&A*, 476, 1113
- romang, S., & Papaloizou, J. 2007, *A&A*, 476, 1123
- Gammie, C. F. 1996, *ApJS*, 457, 355
- Goldreich, P., & Ward, W. R. 1973, *ApJS*, 183, 1051
- Hawley, J. F., Gammie, C. F., & Balbus, S. A. 1995, *ApJ*, 440, 742
- Hawley, J. F., Gammie, C. F., & Balbus, S. A. 1996, *ApJS*, 464, 690
- Ida, S., Guillot, T., & Morbidelli, A. 2008, *ApJ*, in press
- Ida, S., & Lin, D. N. C. 2004, *ApJ*, 604, 388
- . 2008, *ApJ*, 673, 487
- . 2008, *ApJ*, in press
- Inaba, S., & Barge, P. 2006, *ApJS*, 649, 415
- Jin, L. 1996, *ApJS*, 457, 798
- Johansen, A., Anderson, A. C., & Brandenburg, A. 2004, *A&A*, 417, 361
- Johansen, A., Klahr, H., & Henning, Th. 2006, *ApJS*, 636, 1121

- Johansen, A., Oishi, J. S., Mac Low, M.-M., Klahr, H., Henning, Th., & Youdin, A. 2007, *Nature*, 448, 1022
- Klahr, H., & Lin, D. N. C. 2005, *ApJS*, 632, 1113
- Kretke, K. A., & Lin, D. N. C. 2007, *ApJ*, 664, L55
- Masset, F. S., D’Angelo, G., & Kley, W. 2006, *ApJS*, 652, 730
- Nakagawa, Y., Sekiya, M., & Hayashi, C. 1986, *Icarus*, 67, 375
- Oishi, J. S., Mac Low, M.-M., & Menou, K. 2007, *ApJS*, 670, 805
- Rice, W. K. M., Lodato, G., Pringle, J. E., Armitage, P. J., & Bonnell, I. A. 2004, *MNRAS*, 355, 543
- Safronov, V. S. 1969, *Evolution of the Protoplanetary Cloud and the Planets*, NASA Tech. Transl. F-677
- Sano, T., & Miyama, S. M. 1999, *ApJS*, 515, 776
- Sano, T., Miyama, S. M., Umebayashi, T., & Nakano, T. 2000, *ApJS*, 543, 486
- Sano, T., Inutsuka, S. M., Turner, N. J. & Stone, J. M. 2004, *ApJS*, 605, 321
- Sekiya, M. 1998, *Icarus*, 133, 298
- Stone, J. M., & Norman, M. L. 1992a, *ApJS*, 80, 753, 1992b, *ApJS*, 80, 791
- Tanaka, H., Takeuchi, T., & Ward, W. 2002, *ApJS*, 565, 1257
- Yabe, T., & Aoki, T. 1991, *Comput. Phys. Comm.*, 66, 219
- Yudin, A. N., & Shu, F. H. 2002, *ApJS*, 580, 494
- Weidenschilling, S. J. 1977, *MNRAS*, 180, 57
- Weidenschilling, S. J., & Cuzzi, J. N. 1993, in *Protostars and Planets III*, 1031-1060
- Wisdom, J., & Tremaine, S. 1988, *AJ*, 95, 925

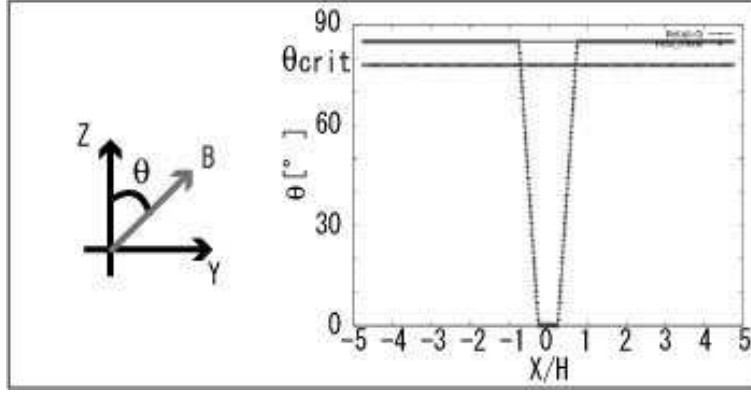


Fig. 1.— The configuration of the initial magnetic field. θ represents the angle from the vertical direction (z) to the azimuthal one (y). It radially varies as shown in the right panel. With constant B_0 , the initial magnetic field is given by $\mathbf{B} = (0, B_0 \sin \theta, B_0 \cos \theta)$. For $\eta = 0.002H^2\Omega_0$, linear calculations suggest that MRI occurs for $\theta < \theta_{\text{crit}} \simeq 79$ degrees.

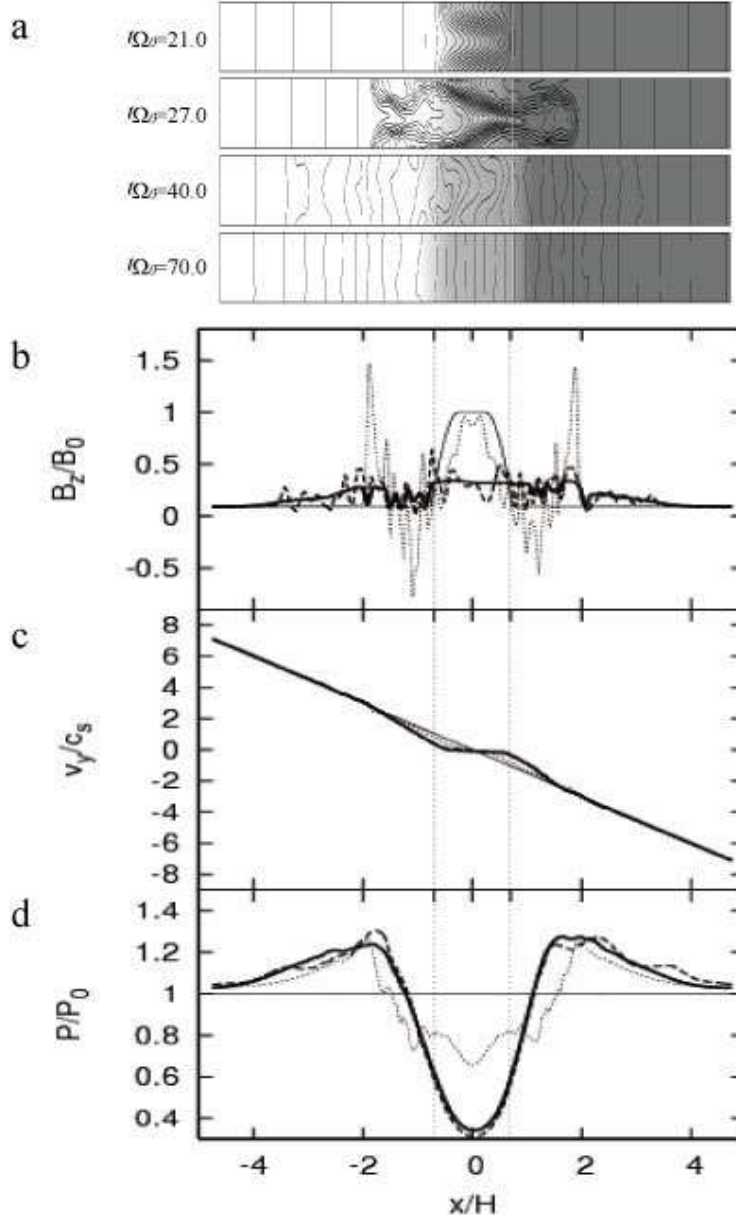


Fig. 2.— Results of the fiducial model. (a) Time evolution of the magnetic field (black lines) and angular velocity v_y (contours) on the x - z plane. The maximum (brightest) or minimum (darkest) of the tone on the contours are set at the unstable and stable region boundaries. Time evolution of vertically averaged values of (b) the vertical magnetic component B_z , (c) angular velocity v_y , and (d) pressure P , as functions of x . In panels (b), (c) and (d), thin solid, dotted, dashed and bold lines express the snapshots at $t\Omega_0 = 0.0, 27.0, 40.0$ and 70.0 , respectively. The unstable region is initially set between the two vertical dotted-lines.

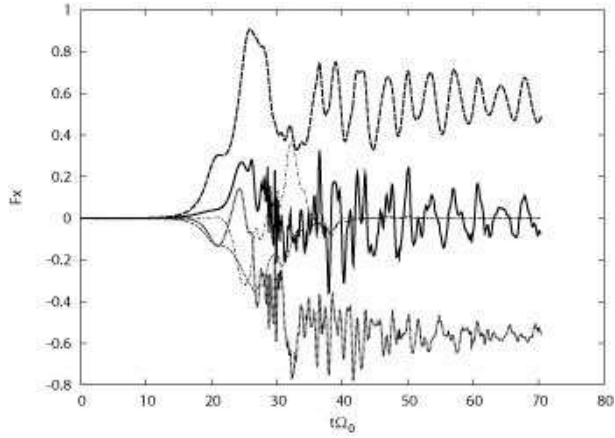


Fig. 3.— Time variation of forces exerted on fluid at $x/H = 0.7$ and $z/H = 0.25$, at which super-Keplerian flow is established. The dotted, dash-dotted, thin dashed and dashed lines express gas radial components of pressure gradient, magnetic pressure gradient, magnetic tension, sum of gravity and Coriolis forces in the r.h.s. of the equation of motion (equation [1]), respectively. The thick solid line is total force. The unit of the forces is $H\Omega_0^2$. The pressure gradient and the gravity/Coriolis forces are dominated and approximately equilibrate with each other.

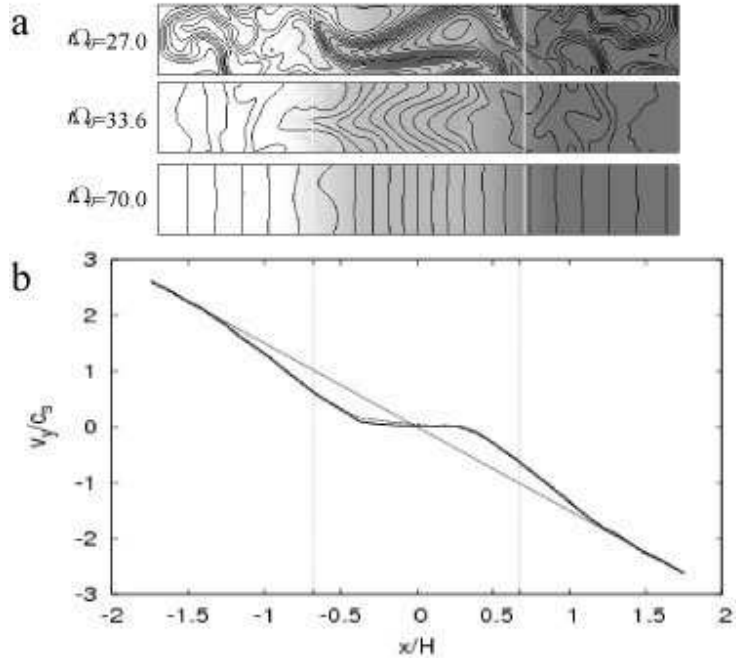


Fig. 4.— Results of model-s11. (a) Time evolution of the magnetic field (solid lines) and angular velocity v_y (contours) on the x - z plane. (b) Time evolution of vertically averaged angular velocity (v_y). The bold, dashed and thin solid lines express the snapshots at $t\Omega_0 = 0.0, 40.0$ and 70.0 , respectively. The meanings of lines are the same as Fig. 2.

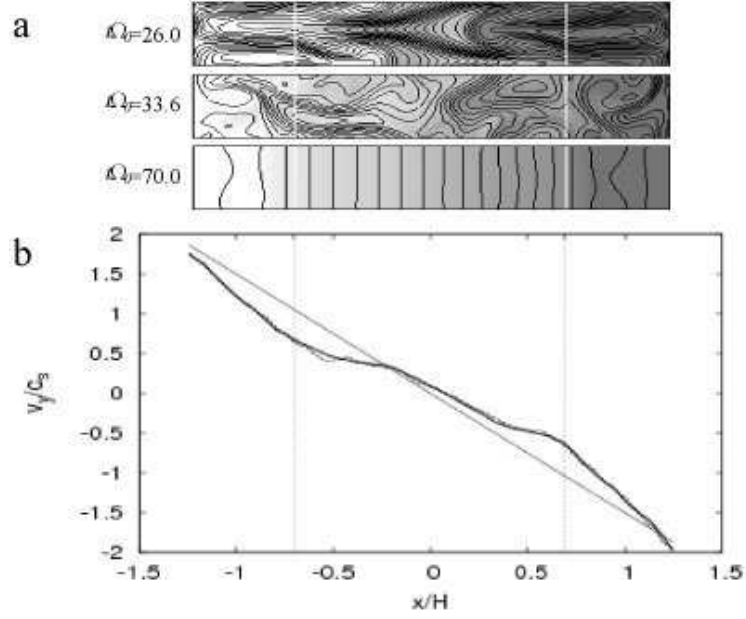


Fig. 5.— The same plots as Fig. 4 except for model-s055.

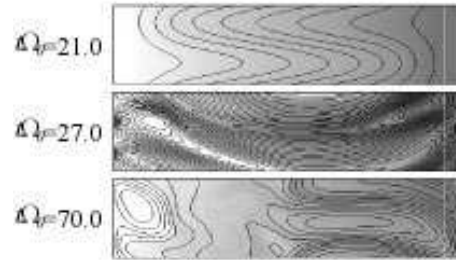


Fig. 6.— The same plots as Fig. 4a except for model-s005.

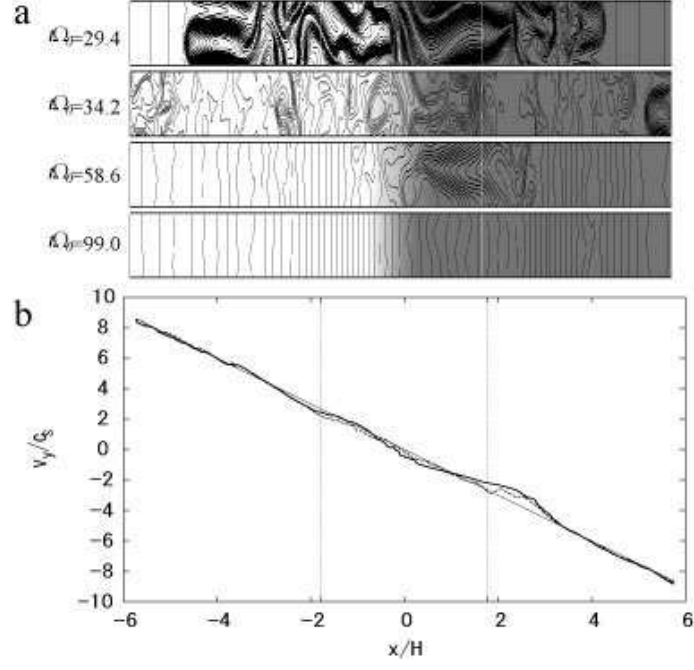


Fig. 7.— The same plots as Fig. 4 except for model-u34.

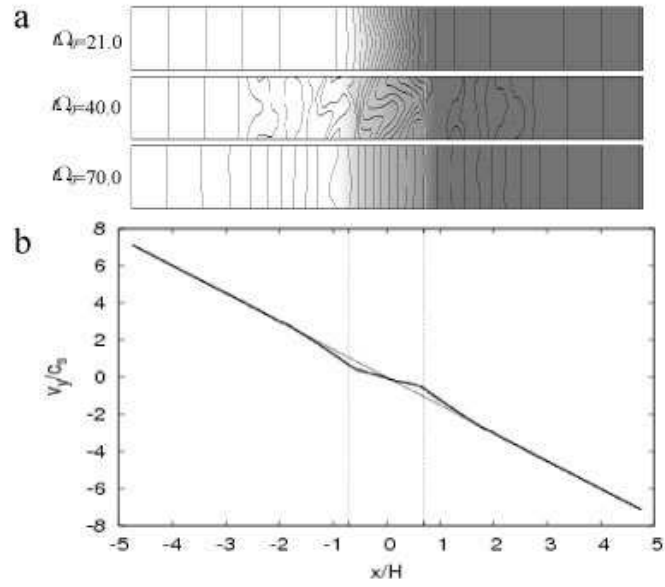


Fig. 8.— The same plots as Fig. 4 except for model- $\eta 0$.

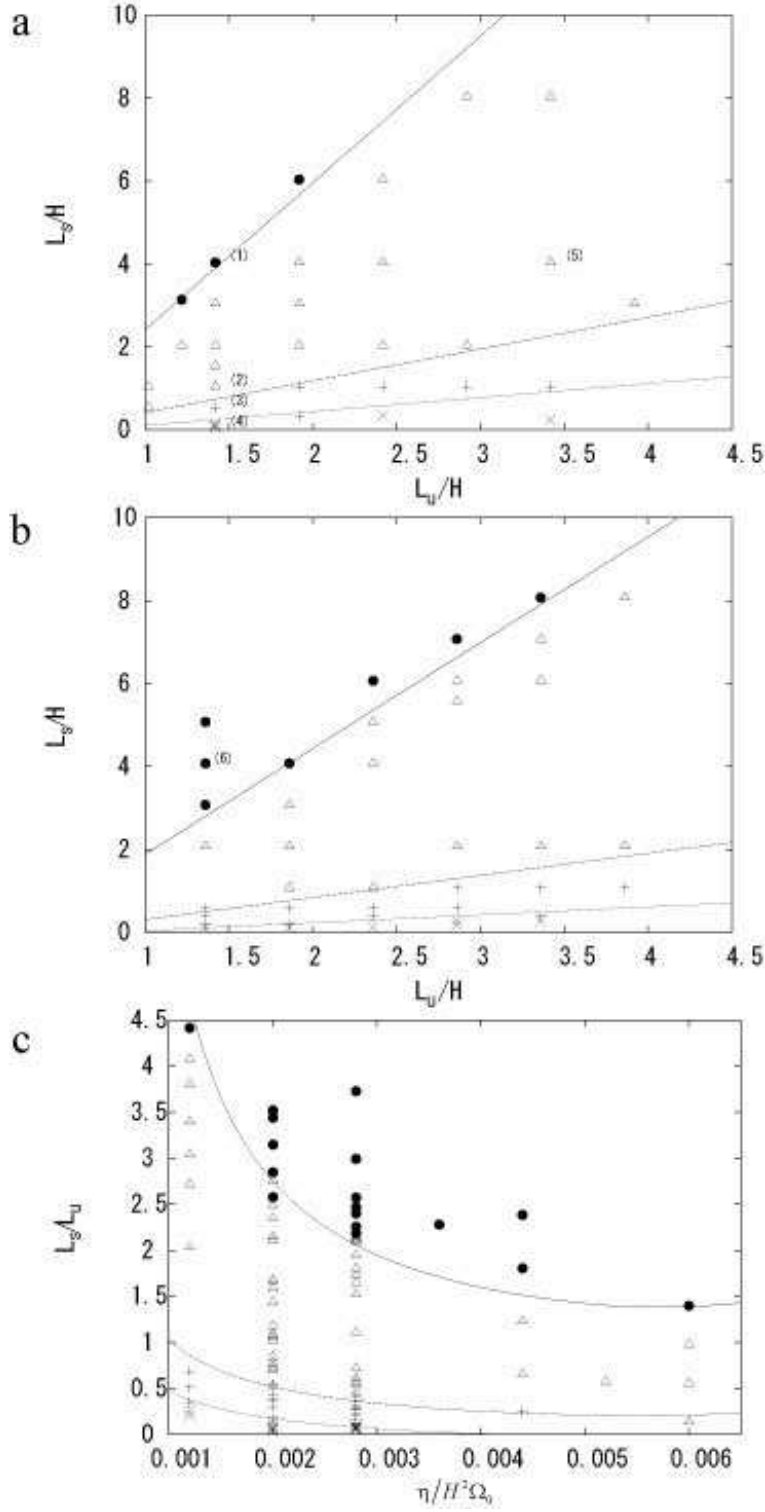


Fig. 9.— The classification of results by the magnetic Reynolds number. Runs with (a) $\eta = 0.0020\Omega_0 H^2$ and (b) $\eta = 0.0028\Omega_0 H^2$ on the $L_u - L_s$ plane and (c) all the runs on the $\eta - L_s/L_u$ plane. The four types of results, A, B, C and D, are represented by filled circles, triangles, daggers and crosses. The solid, dashed and dotted lines express $R_{m,ave} = 0.1, 0.5$ and 1.0 respectively. The runs with numbers express (1)fiducial model; (2)model-s11; (3)model-s054; (4)model-s005 (5)model-u34; (6)model- $\eta 0$.

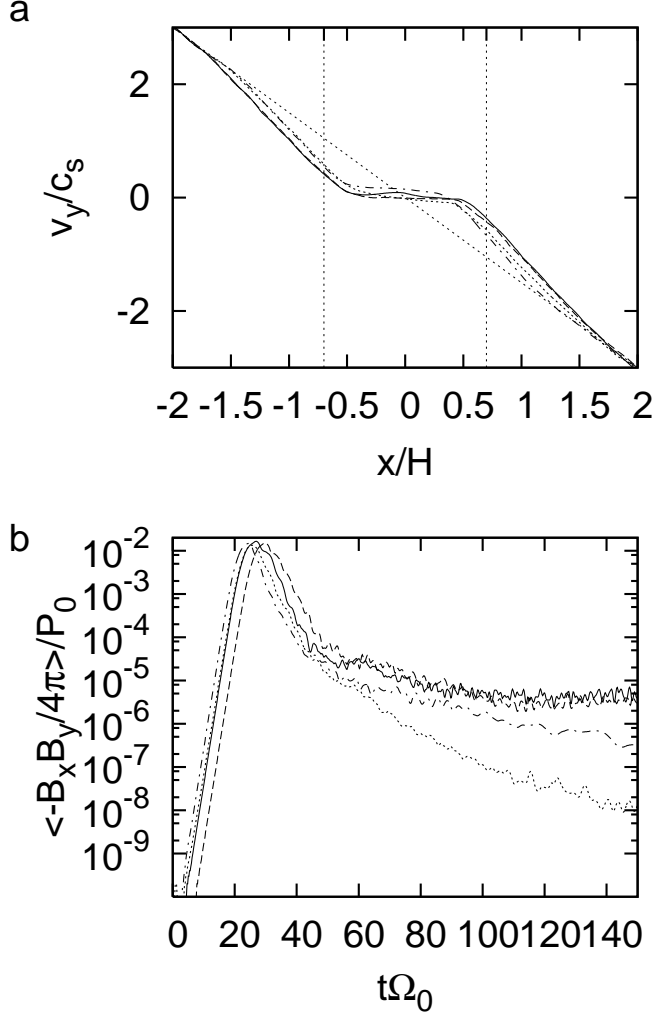


Fig. 10.— Results for various resolutions. (a) Close-up snapshots of vertically averaged angular velocity (v_y) at $t\Omega_0 = 150.0$. (b) Time evolution of the volume-averaged Maxwell stress which is normalized by the initial pressure P_0 . Resolutions corresponding to $dx = dz = 0.005H$, $0.01H$, $0.0156H$ and $0.025H$ are represented by dashed, bold, dash-dotted and dotted lines respectively.

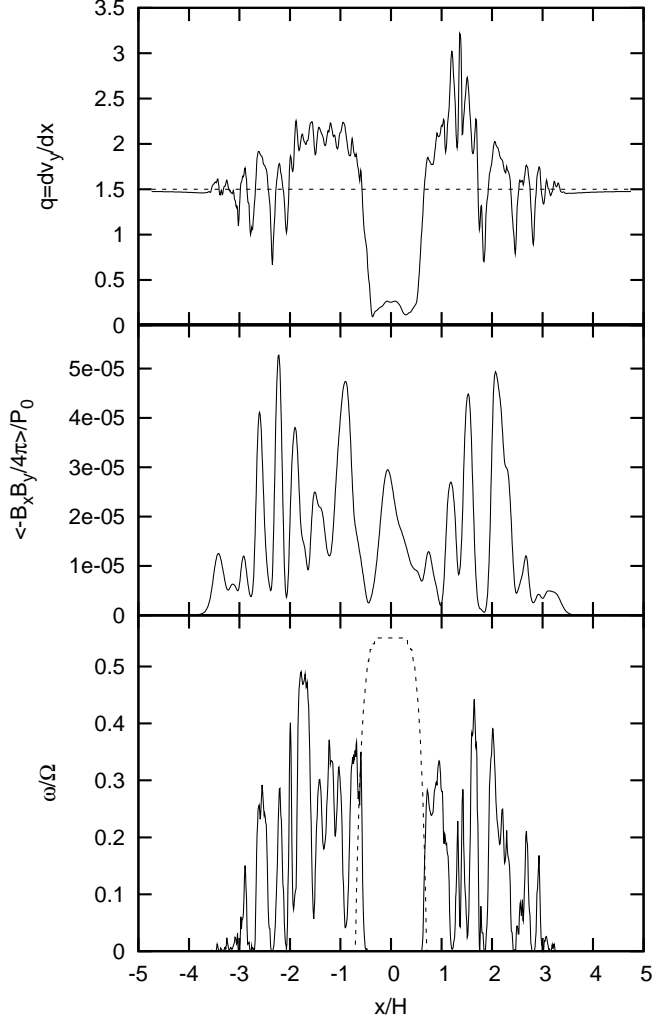


Fig. 11.— Temporally and vertically averaged shear rate $q = -dv_x/dt$ (*top*), Maxwell stress normalized by initial pressure $-\langle B_x B_y \rangle / 4\pi P_0$ (*middle*) and the growth rate estimated by the dispersion relation (equation (2) in Appendix 2) with the simulated values (*bottom*) of the fiducial model. Bold lines are values temporally averaged over $t\Omega_0 = 45.0 - 70.0$ and dashed lines mean the initial values.

$\eta/\Omega_0 H^2$	L_u/H	L_s/H	$R_{m,ave}$	result	$\Delta v_y/c_s$
0.0012	1.5	6.5, 6.0, 5.0, 4.0	0.10, 0.11, 0.13, 0.16	A, B, B, B	0.82, 1.2, 0.91, 0.86
		1.0, 0.51	0.61, 1.1	C, C	0.66, 0.51
	2.0	7.5, 6.0, 4.0	0.13, 0.16, 0.23	B, B, B	1.7, 1.1, 0.98
		1.0, 0.51	0.89, 1.4	C, D	0.68, ...
	2.5	0.51	1.7	D	...
0.002	1.0	1.1, 0.54	0.23, 0.42	B, B	0.40, 0.38
	1.2	3.1	0.10	A	0.57
	1.4	4.0 ¹ , 3.1, 1.1 ² , 0.55 ³	0.096, 0.13, 0.37, 0.64	A, B, B, C	0.73, 0.55, 0.48, 0.41
		0.15, 0.10, 0.05 ⁴	1.2, 1.4, 1.5	D, D, D	..., ..., ...
	1.9	6.0, 4.0, 3.0	0.094, 0.14, 0.19	A, B, B	0.97, 0.88, 0.54
		2.0, 1.0, 0.35	0.28, 0.53, 1.1	B, C, C	0.87, 0.72, 0.43
	2.4	2.0, 0.35	0.38, 1.3	B, D	1.2, ...
	2.9	10.0, 8.0, 1.0	0.092, 0.11, 0.81	A, B, C	1.2, 1.4, 0.99
	3.4	12.0, 8.0, 4.0 ⁵ , 0.24	0.090, 0.14, 0.28, 1.8	A, B, B, D	1.0, 1.2, 1.1, ...
	3.9	3.1	0.44	B	0.77
0.0028	1.4	5.1, 4.0 ⁶ , 2.1, 0.57	0.15, 0.069, 0.14, 0.45	A, A, B, C	0.35, 0.45, 0.28, 0.23
		0.37, 0.17, 0.11	0.61, 0.87, 1.00	C, C, D	0.34, 0.14, ...
	1.9	4.0, 3.1, 2.1, 1.1	0.099, 0.14, 0.20, 0.38	A, B, B, B	0.48, 0.31, 0.49, 0.42
		0.57, 0.17, 0.11	0.61, 1.05, 1.2	C, C, D	0.40, 0.25, ...
	2.4	6.1, 5.1, 4.0, 1.1	0.088, 0.11, 0.13, 0.49	A, B, B, B	0.50, 0.62, 0.66, 0.53
		0.57, 0.37, 0.11	0.75, 0.92, 1.25	C, C, D	0.46, 0.28, ...
	2.9	7.1, 6.1, 5.1, 2.1	0.093, 0.11, 0.12, 0.47	A, B, B, B	0.60, 0.42, 0.50, 0.48
		1.1, 0.57, 0.27, 0.17	0.58, 0.85, 1.13, 1.26	C, C, D, D	0.56, 0.37, ..., ...
	3.4	8.1, 7.1, 6.1, 2.1	0.0097, 0.11, 0.13, 0.39	A, B, B, B	1.00, 0.79, 0.58, 0.78
		1.1, 0.37, 0.27	0.66, 1.1, 1.3	C, C, D	0.48, 0.61, ...
	3.9	8.1, 2.1, 1.1	0.11, 0.45, 0.73	B, B, B	0.46, 0.43, 0.49
0.0036	1.8	4.1	0.077	A	0.28
0.0044	1.7	4.1, 3.1	0.063, 0.085	A, A	0.17, 0.18
		2.1, 1.1, 0.43	0.13, 0.24, 0.50	B, B, B	0.20, 0.18, 0.18
0.0052	2.3	1.3	0.24	B	0.15
0.0060	2.4	3.3, 2.3, 1.3, 0.32	0.084, 0.36, 0.21, 0.50	A, B, B, B	0.22, 0.17, 0.21, 0.20

Table 1: Simulation parameters and results for 91 runs. η , L_u , L_s , $R_{m,ave}$, and Δv are magnetic resistivity, radial width of unstable region, that of stable regions, initial averaged magnetic Reynolds number and the maximum deviation from Kepler velocity, respectively. For highly turbulent cases (marked “D”), Δv_y is omitted. The fifth column “result” indicates classification of the results (§3.3). Multiple values in the columns correspond to different runs. (1) fiducial model; (2) model-s11; (3) model-s055; (4) model-s005; (5) model-u34; (6) model- $\eta 0$.